Supplementary Information

Effective Separating of Metal Impurities from Gypsum Nanosludge: Synergism of Mechanical Force and Metal Species Regulation

Changzhou Weng[a, c], Zhengqiang Zheng[a, c], Chen Tian[b, d *], Zhang Lin[b, c *]

a School of Environment and Energy, Guangdong Provincial Key Laboratory of Solid Wastes Pollution Control and Recycling, South China University of Technology, Guangzhou, Guangdong 510006, China.

b Chinese National Engineering Research Center for Control and Treatment of Heavy Metal Pollution, School of Metallurgy and Environment, Central South University, Changsha, Hunan 410083, China.

c The Key Laboratory of Pollution Control and Ecosystem Restoration in Industry Clusters (Ministry of Education), South China University of Technology, Guangzhou, Guangdong 510006, China.

d School of Future Membrane Technology, Fuzhou University, Fuzhou, 350108, China

This PDF file includes:

Contents

Materials and Methods

S1. Inductive coupled plasma-optical emission spectroscopy (ICP-OES)

The concentrations of released metals were quantified using Inductively Coupled Plasma Optical Emission Spectrometry (ICP-OES) on an Agilent 730 spectroscope. Prior to analysis, the leaching solutions were acidified with nitric acid (HNO_3) to achieve a pH range of 2–3. To determine the metal content in solid samples, the solids were fully dissolved in HNO_3 (adjusted to pH = 1.0), and the resulting digestion solution was then diluted to a constant volume with deionized water. The metal concentrations in these digestion solutions were measured, and the metal content in the solid samples was calculated accordingly.

S2. Analysis of impurities / metals incorporation via the Rietveld refinement method

Mineral identification and quantification in gypsum were conducted through X-ray diffraction (XRD) analysis using a Bruker D8 Advance diffractometer equipped with a Cu-Kα radiation source (operating at 40 kV and 40 mA) and a LynxEye XE array detector. The XRD patterns were collected over a 2θ range of 5° to 80°, with a step size of 0.02° / 0.01° and a counting time of 0.2-2.0 seconds per step. Mineral phases were identified by matching patterns against the PDF 2004 and COD 2010 databases from the International Centre for Diffraction Data (ICDD) and Crystallography Open Database (COD), respectively, using X'Pert HighScore Plus software. Metal incorporation analysis within gypsum was performed using the Rietveld refinement method in DIFFRAC.TOPAS (version 5.0, Bruker). For quantitative phase analysis, raw structure files from COD were utilized, and modifications to the chemical formulas in these files were made based on microstructural analysis to account for metal incorporation[1].

S3. Other microscopic characterization

TEM observations and selective area electronic diffraction (SAED) of the samples were

performed on a FEI Talos F200X microscope. Elemental mappings and line profiles were tested on a SuperXG2 energy dispersive X-ray spectroscopy. Scanning electronic microscopy (SEM) was conducted on a Hitachi SU8100 field emission microscope.

S4. Metal-doping content conversion rate

As shown in **Figure S2, Figure S11 and Figure S12**, the equation provided describes the conversion rate of metal transitioning from a doped state to an undoped state in gypsum samples. Here is a detailed breakdown of the parameters and how the calculation works:

Equation:

$$D = \frac{d_{raw} - d_{treat}}{d_{raw}} \times 100\%$$

Parameters:

- D, Metal-doping content conversion rate (%). This value indicates the percentage change from the initial metal-doped state in the raw gypsum to the treated state after milling or calcination.
- d_{raw}, Metal-doping content of the raw gypsum (%). This parameter represents the initial amount of metal content present in the untreated gypsum samples.
- d_{treat}, Metal-doping content of milled or calcined products (%). This reflects the remaining metal content in the gypsum after the treatment process (milling or calcination).

Interpretation:

- The equation essentially measures the reduction in metal-doping content as a fraction of the original metal-doping content, indicating the efficiency of the milling or calcination treatment in excluding the doped metals from the gypsum matrix.
- A higher value of D suggests a more effective conversion of metals from the doped to the undoped state, reflecting effectively metal exclusion during the treatment process.

S5. DFT details

In this study, all computational work was performed using the Vienna Ab initio Simulation Package (VASP)[2] with the projector augmented wave (PAW) method[3]. The Perdew-Burke-Ernzerhof (PBE)[2] functional within the generalized gradient approximation (GGA) was employed for the exchange-correlation functional, supplemented by the DFT-D3 correction[4] for dispersion interactions. A plane-wave cut-off energy of 500 eV was applied, and a 15 Å vacuum layer was introduced for all surface models to avoid interactions between periodic images. Brillouin zone sampling was conducted using a 4×4×1 Gamma-centre kpoint sampling. The convergence criterion for self-consistent field calculations was set to 10^{-5} eV, and atomic positions were optimized until the maximum force on any atom was below 0.02 eV/Å.

The primitive unit cells of calcium sulphate dihydrate (DH, $CaSO_4 \cdot 2H_2O$) and calcium sulfate hemihydrate (HH, $CaSO_4 \cdot 0.5H_2O$) were optimized first, and their lattice parameters were determined. The (020) and (200) surfaces were cleaved from the optimized structures of DH and HH, respectively, representing the most exposed surfaces[5,6].

The binding energy (E_b) for adsorbate incorporation into the substrate was calculated using the following equation:

$$E_b = E_{sur+adsorbate} - E_{sur} - E_{adsorbate}$$

Where,

- $E_{sur+adsorbate}$ is the total energy of adsorption model;
- E_{sur} is the total energy of surface;
- $E_{adsorbate}$ is the total energy of adsorbate.

S6. The Gibbs free energy change (ΔG)

The Gibbs free energy change (ΔG) for a reaction is calculated using the equation:

$$\Delta G = \Delta G^{\theta} + RT\ln Q$$

- ΔG^{θ} is the standard Gibbs free energy change, which can be obtained from standard Gibbs free energies of formation (ΔG_f, list in **Table S5**) for reactants and products.
- **R** is the gas constant (8.314 $J \cdot mol^{-1} \cdot K^{-1}$).
- **T** is the temperature in Kelvin, typically assumed to be 298 K unless stated otherwise.
- **Q** is the reaction quotient, calculated based on the concentrations of the reactants and products

Cupric ions (Cu^{2+}) are unstable in thiosulfate solutions, particularly in sodium thiosulfate, due to rapid redox reactions with $S_2O_3^{2-}$, as outlined in **Reaction S1**, resulting in the formation of Cu^{+} that cannot sustain the Cu^{2+} state for long[7].

Reaction S1:

$$2Cu^{2+} + 8S_2O_3^{2-} = 2Cu(S_2O_3)_3^{5-} + S_4O_6^{2-} \qquad \triangle G_{S1} = -162.1\ kJ \cdot mol^{-1}$$

According to the speciation diagram analysis conducted by Han et al.[8], $Cu(S_2O_3)_3^{5-}$ ions are likely the primary copper species present in thiosulfate solutions. It is hypothesized that two moles of Cu^{+} ions can be substituted by one mole of Hg^{2+} ions through the **Reaction S2** described below.

Reaction S2:

$$Hg^{2+} + 2Cu(S_2O_3)_3^{5-} = 2Cu^{+} + Hg(S_2O_3)_4^{6-} + 2S_2O_3^{2-} \qquad \triangle G_{S2} = -33.35\ kJ \cdot mol^{-1}$$

The calculated Gibbs free energy changes for **Reaction S1** and **Reaction S2** are -162.1 kJ/mol and -33.35 kJ/mol, respectively. The highly negative Gibbs free energy of **Reaction S1** indicates that it proceeds spontaneously and completely. **Reaction S2**, with a Gibbs free energy of -33.35 kJ/mol, also proceeds spontaneously but at a lower magnitude compared to **Reaction S1**.

Figures

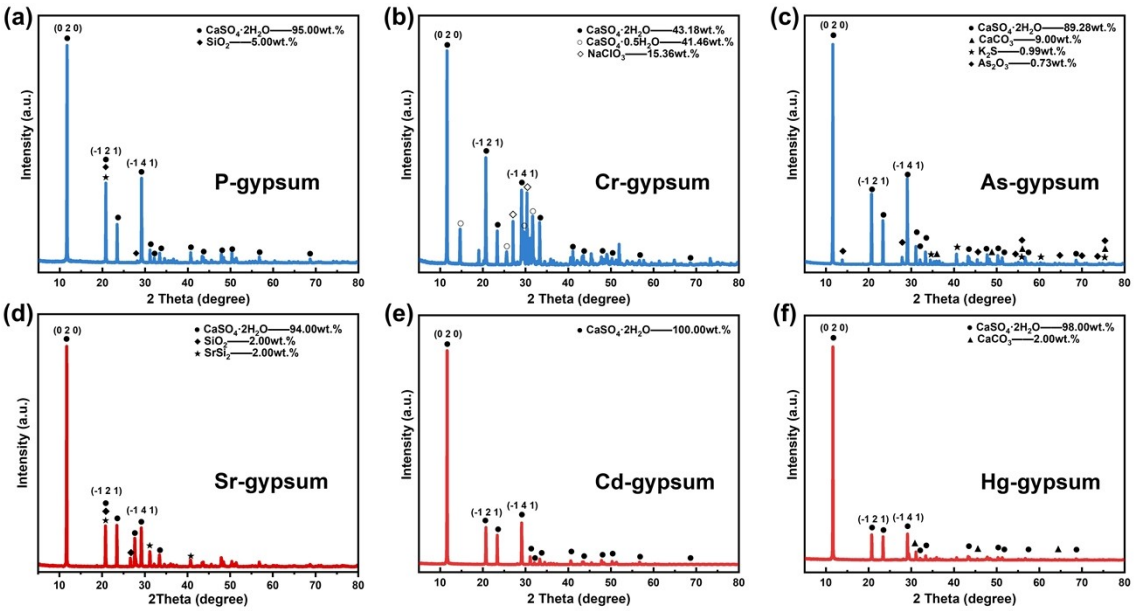

Figure S1. XRD results of the original gypsum samples.

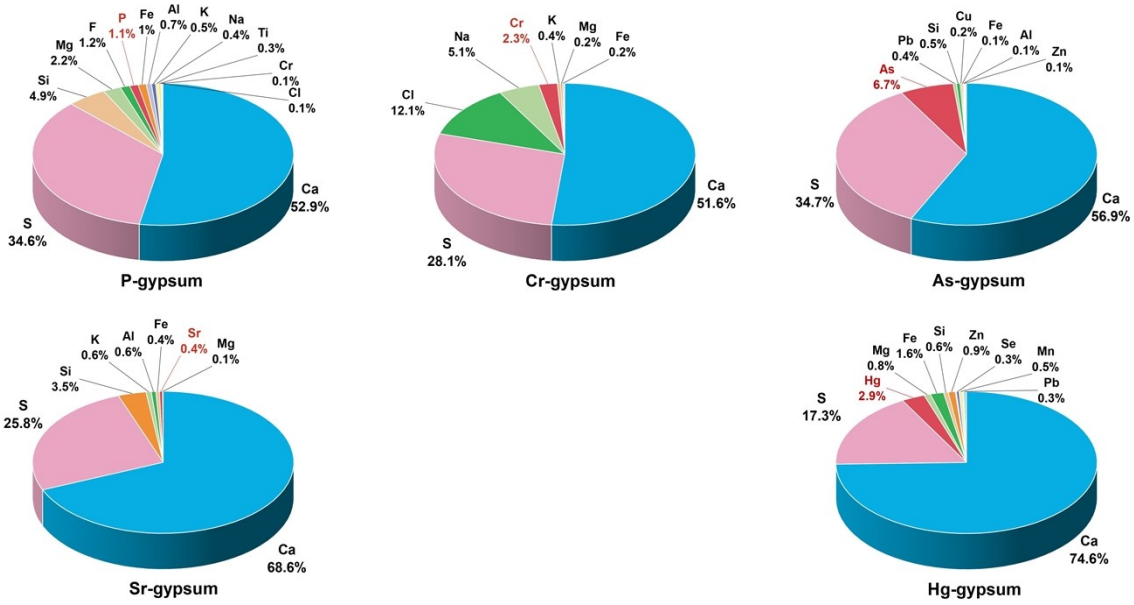

Figure S2. XRF results of the original gypsum samples.

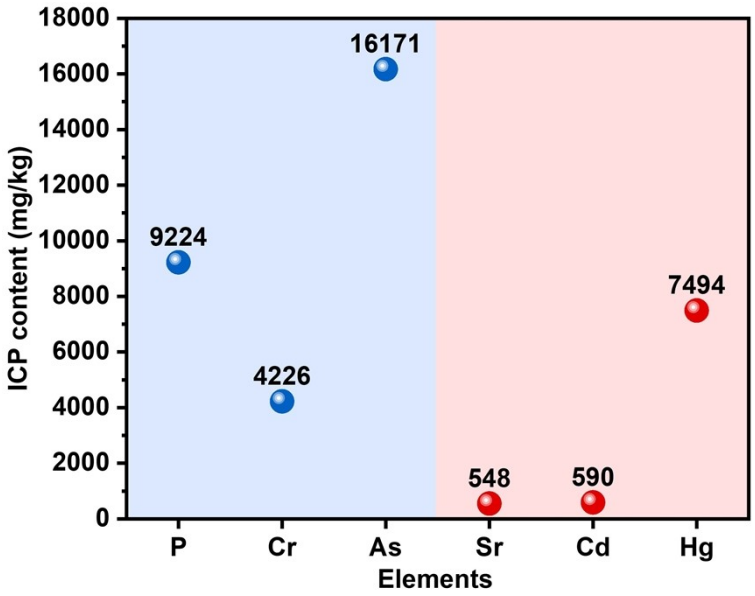

Figure S3. ICP results of the original gypsum samples.

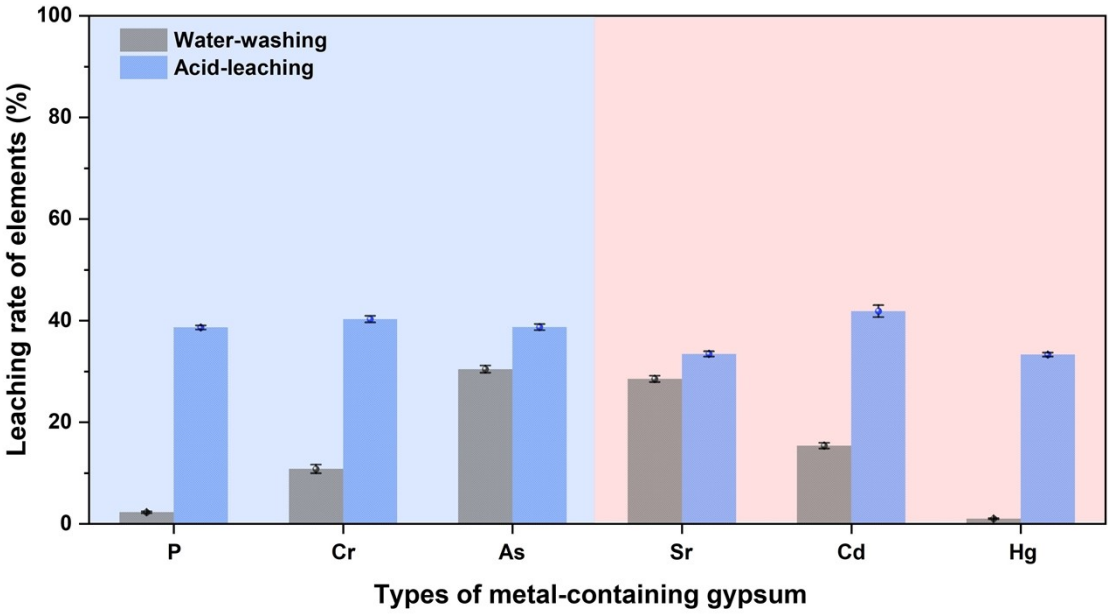

Figure S4. Leaching rate of elements in the original gypsum samples after water-washing and acid-leaching.

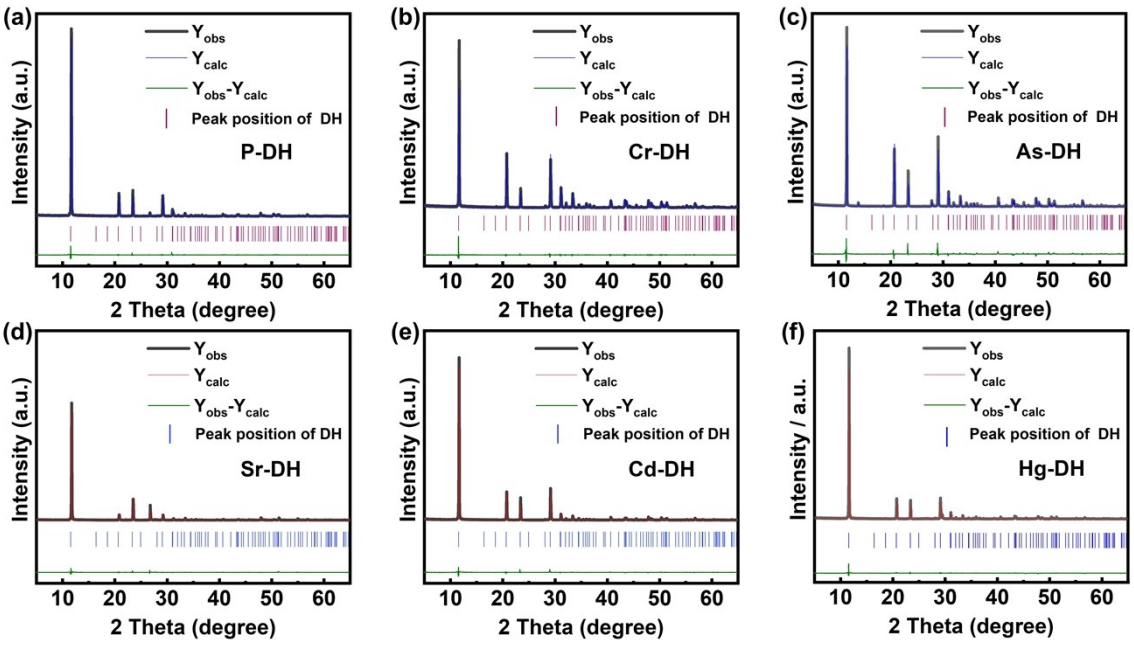

141

142 **Figure S5.** Rietveld refinement of XRD patterns for (a) P-DH, (b) Cr-DH, (c) As-DH, (d) Sr-

143 DH, (e) Cd-DH, and (f) Hg-DH.

144

The XPS analysis presented in **Figure S6** provides insight into the valence states and chemical forms of the various elements incorporated into the gypsum samples.

Figure S6a: The spectrum displays peaks at 133.65 eV and 134.95 eV, corresponding to P^{5+} $2p_{3/2}$ and $2p_{1/2}$, respectively, indicating the presence of pentavalent phosphorus[9,10].

Figure S6b: The weak Cr 2p signals in Cr-gypsum are attributed to the low chromium content. However, two peaks at 579.8 eV and 589.1 eV were observed, indicating the presence of Cr(VI), likely as CrO_4^{2-}, since $Cr_2O_7^{2-}$ is less probable under alkaline wastewater conditions[11].

Figure S6c: For arsenic-doped gypsum, As 3d peaks were fitted at 44.7 eV and 44.2 eV, corresponding to As^{5+} and As^{3+}, respectively. The prominent presence of As^{5+} observed in XPS analysis, coupled with the FT-IR and Raman data presented in the surrounding context, indicates that arsenic primarily exists in its pentavalent state, most likely in the form of $HAsO_4^{2-}$[12].

Figure S6d: Sr $3d_{5/2}$ and Sr $3d_{3/2}$ peaks appear at 133.84 eV and 135.35 eV, respectively, confirming the presence of Sr^{2+} in Sr-gypsum[10].

Figure S6e: Cd 3d spectra display two peaks at 405.54 eV (Cd $3d_{5/2}$) and 412.35 eV (Cd $3d_{3/2}$), with a separation of 6.8 eV, which is characteristic of cadmium compounds[13].

Figure S6f: The spectrum shows the deconvoluted Hg 4f spectrum for Hg-gypsum, with Hg^{2+} $4f_{7/2}$ peaks at 100.04 eV and 102.11 eV, and Hg^{2+} $4f_{5/2}$ at 104.04 eV, consistent with literature values for mercury compounds[8,14,15].

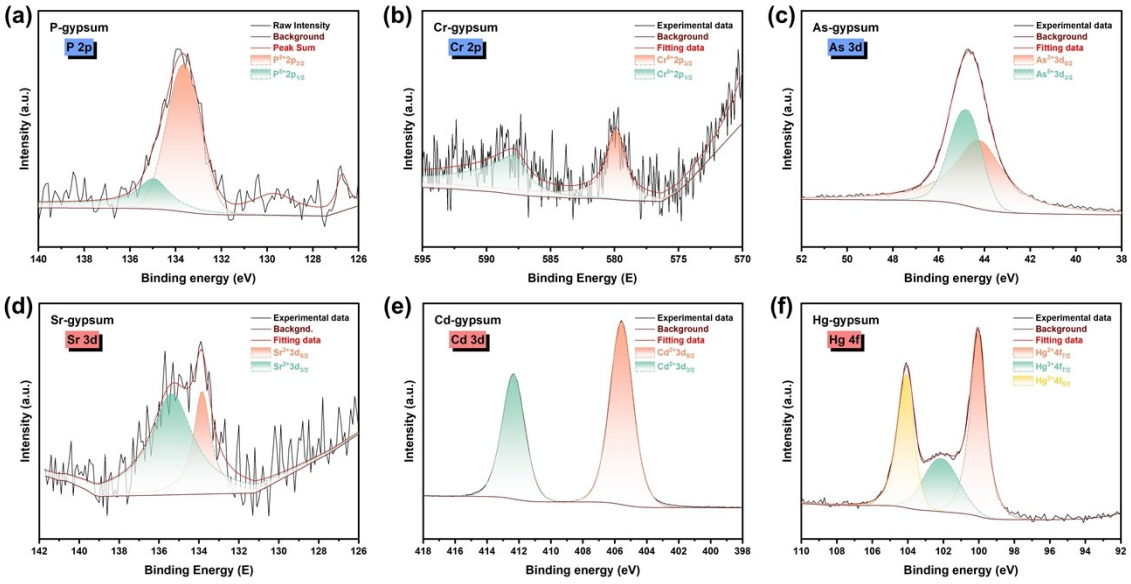

Figure S6. XPS spectra of (a) P-DH, (b) Cr-DH, (c) As-DH, (d) Sr-DH, (e) Cd-DH, and (f) Hg-DH.

The FT-IR spectra presented in **Figure S7** provide insight into the vibrational modes of functional groups in the various gypsum samples, with significant differences observed between pure gypsum and doped samples.

In the FT-IR spectrum of pure gypsum, characteristic sulfate ion vibrations (SO_4^{2-}) are observed at 1004 cm^{-1} (ν_1), 464 cm^{-1} (ν_2), 1128 cm^{-1} (ν_3), 671 cm^{-1} (ν_4), and 601 cm^{-1} (ν_4)[16]. The bending mode of H_2O molecules is observed at 1683 cm^{-1} (ν_2) and 1621 cm^{-1} (ν_2), with the stretching vibrations of crystal water appearing at 3521 cm^{-1} (ν_3) and 3403 cm^{-1} (ν_1)[17,18].

Figure S7a: In the P-gypsum sample, additional peaks at 1450 cm^{-1} are assigned to C-H stretching vibrations, indicating the presence of organic impurities. A distinct peak at 879 cm^{-1} can be attributed to the presence of HPO_4^{2-}, suggesting phosphate incorporation into the gypsum matrix[19].

Figure S7b: For the Cr-gypsum sample, notable changes are observed compared to pure gypsum. The peaks at 2240 cm^{-1} and 2116 cm^{-1} correspond to the stretching vibrations of C≡N bonds, likely indicating the presence of nitrile compounds. A new, sharp peak at 878 cm^{-1} is assigned to the CrO_4^{2-} group, confirming the incorporation of chromium in the form of chromate[20].

Figure S7c: The peak at 703 cm^{-1} of As-gypsum corresponds to the As-OH stretching vibration, indicating the presence of $HAsO_4^{2-}$ species within the sample. The absence of FTIR bands between 750 and 860 cm^{-1} suggests that AsO_4^{3-} species are not present within the gypsum structure[21]. Based on the correlation between As content in gypsum and As(V) species, it can be concluded that $HAsO_4^{2-}$ incorporated into the gypsum lattice.

Figure S7d: In the FT-IR spectrum of Sr-gypsum, additional peaks at 2242 cm^{-1} and 2121 cm^{-1} correspond to the C≡N stretching vibrations, similar to the Cr-gypsum spectrum. Furthermore, peaks at 788 cm^{-1} and 778 cm^{-1} can be attributed to the C-H stretching vibrations, suggesting the presence of organic contaminants[22]. The sulfate and water vibrations remain largely unaltered, though slight shifts in peak positions may indicate minor structural perturbations due to the incorporation of Sr^{2+} into the gypsum matrix.

Figure S7e: The FT-IR spectrum of Cd-gypsum reveals peaks at 2214 cm^{-1} and 2116 cm^{-1}, again indicating the presence of C≡N stretching vibrations, as seen in other doped samples. A new peak at 857 cm^{-1} corresponds to Cd-O-H bending vibrations, suggesting cadmium incorporation

into the gypsum structure[23]. Additionally, the absorption peaks at 1452 cm^{-1} and 1084 cm^{-1} indicate the presence of CO_3^{2-}, suggesting that carbonate ions may have been incorporated into the sample[24].

Figure S7f: The Hg-gypsum sample shows significant modifications in the FT-IR spectrum. Peaks at 671 cm^{-1}, 602 cm^{-1}, and 458 cm^{-1} correspond to Hg^{2+} interactions, while peaks at 1447 cm^{-1} and 874 cm^{-1} are assigned to the carbonate ion (CO_3^{2-})[25]. Additionally, peaks at 2920 cm^{-1} and 2855 cm^{-1} indicate the presence of carbonate species, likely due to secondary mineral formation. The sulfate and water vibrations are present, but some peak broadening suggests structural changes induced by mercury incorporation[26].

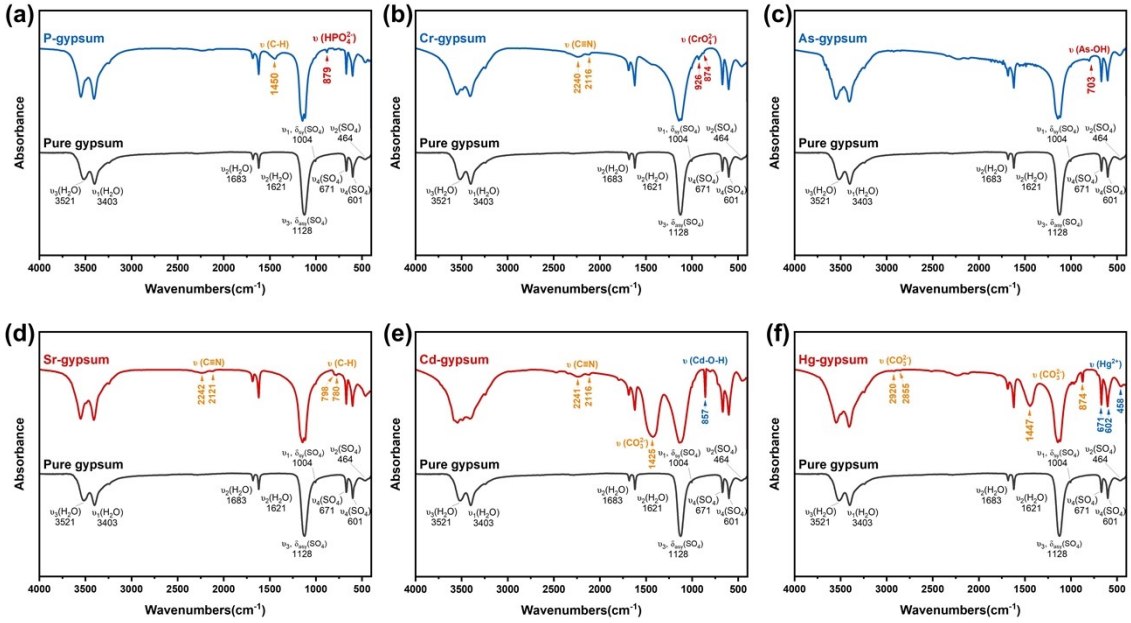

Figure S7. FT-IR spectra of (a) P-DH, (b) Cr-DH, (c) As-DH, (d) Sr-DH, (e) Cd-DH, and (f) Hg-DH. The peak which is different from pure gypsum is marked in the figure.

The Raman spectra provide valuable insights into the incorporation of impurities into the gypsum structure, as illustrated in **Figure S8**.

Figure S8a: In the Raman spectrum of the initial phosphogypsum (P-gypsum) sample, peaks at 1334 cm^{-1} and 1611 cm^{-1} are attributed to the stretching and deformation vibrations of C=C bonds, respectively, which likely arise from organic impurities or residuals commonly found in phosphogypsum[27].

Figure S8b: Comparing the Raman spectrum of Cr-gypsum with pure gypsum, a distinct peak at 878 cm^{-1} was observed. This signal aligns closely with the reported stretching vibrations of CrO_4^{2-} (853-906 cm^{-1}) in the literature, confirming the presence of chromate ions in the sample. The absence of characteristic $Cr_2O_7^{2-}$ signals (911-959 cm^{-1}) further support this conclusion[28]. Additionally, a peak at 673 cm^{-1} could indicate structural disorder caused by the incorporation of chromium ions into the gypsum[29].

Figure S8c: For As-gypsum, the peak around 674 cm^{-1} is noteworthy when compared to pure gypsum. This band is typically associated with structural disorder within the crystal lattice, which suggests arsenic incorporation. This incorporation is likely causing distortions within the gypsum matrix, which is manifested as an additional Raman feature[30].

Figure S8d: The Raman spectrum of Sr-gypsum shows peaks at approximately 1434 cm^{-1}, 1603 cm^{-1}, and 1758 cm^{-1}, which are absent in pure gypsum. The peak at 1434 cm^{-1} may correspond to interactions between Sr^{2+} and surrounding sulfate groups (SO_4^{2-}) or water molecules[31]. The signal at 1603 cm^{-1} could be linked to Si-O bond vibrations from the SiO_2 impurities present in the sample. The peak at 1758 cm^{-1} likely results from Sr^{2+} interactions with other components in the crystalline structure, such as water molecules or sulfate ions. Overall, these distinct signals are indicative of Sr^{2+} incorporation into the gypsum matrix, altering both the crystal structure and the vibrational behavior of water and SO_4^{2-} ions.

Figure S8e: In Cd-gypsum, the peaks observed at 670 cm^{-1} and 1084 cm^{-1} are likely associated with Cd^{2+} incorporation, indicating structural perturbations related to the presence of cadmium[32,33].

Figure S8f: For Hg-gypsum, a peak at approximately 279 cm^{-1} is observed, which may be attributed to HgS (mercury sulfide) formation. Additionally, the peak at 1087 cm^{-1} corresponds to carbonate (CO_3^{2-}) stretching vibrations, indicating the potential presence of calcium carbonate[34].

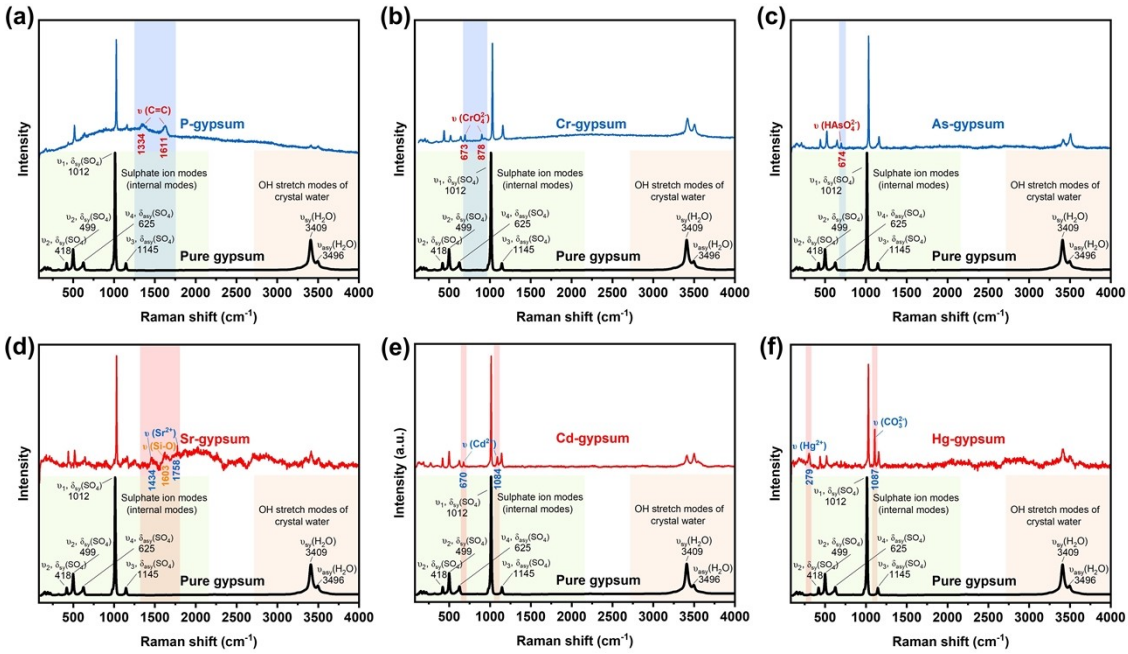

Figure S8. Raman spectra of (a) P-DH, (b) Cr-DH, (c) As-DH, (d) Sr-DH, (e) Cd-DH, and (f) Hg-DH. The peak which is different from pure gypsum is marked in the figure.

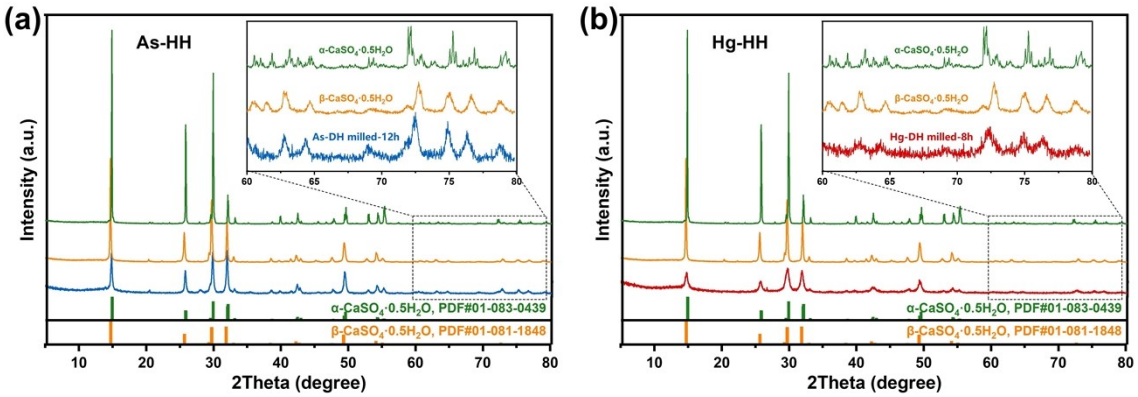

Figure S9. X-ray diffraction (XRD) patterns of α-$CaSO_4 \cdot 0.5H_2O$ and β-$CaSO_4 \cdot 0.5H_2O$ compared with (a) As-HH and (b) Hg-HH prepared via ball-milling.

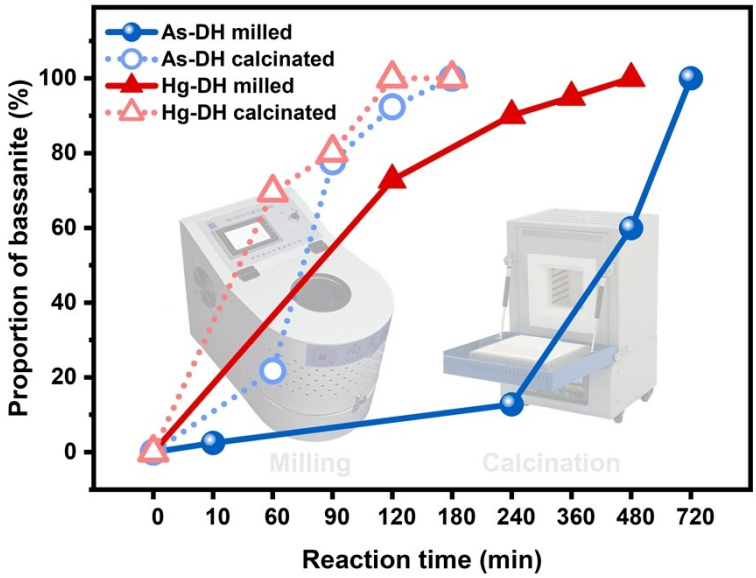

Figure S10. Proportion of bassanite in As-DH and Hg-DH after ball-milling at room temperature or calcination at 120°C for different time.

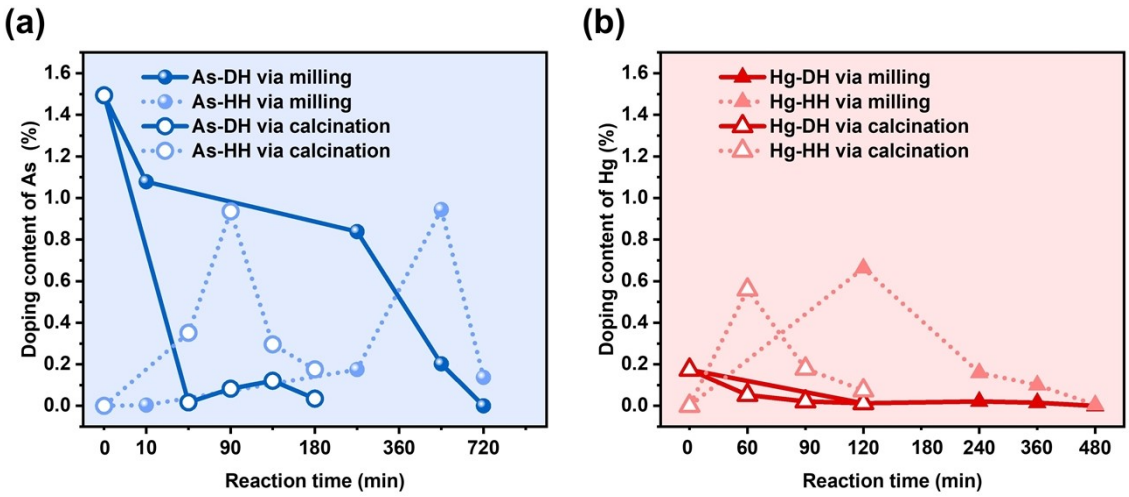

Figure S11. Metal doping content in the products of (a) As-DH and (b) Hg-DH treated through ball-milling or calcination at different times.

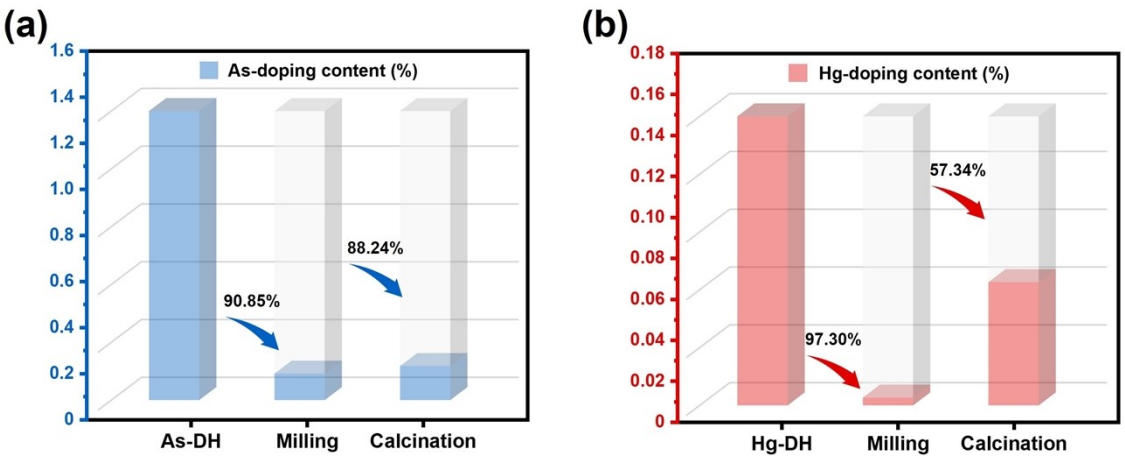

253

254 **Figure S12.** Metal doping content changes in the hemihydrate products of (a) As-DH and (b)

255 Hg-DH treated by milling or calcination.

256

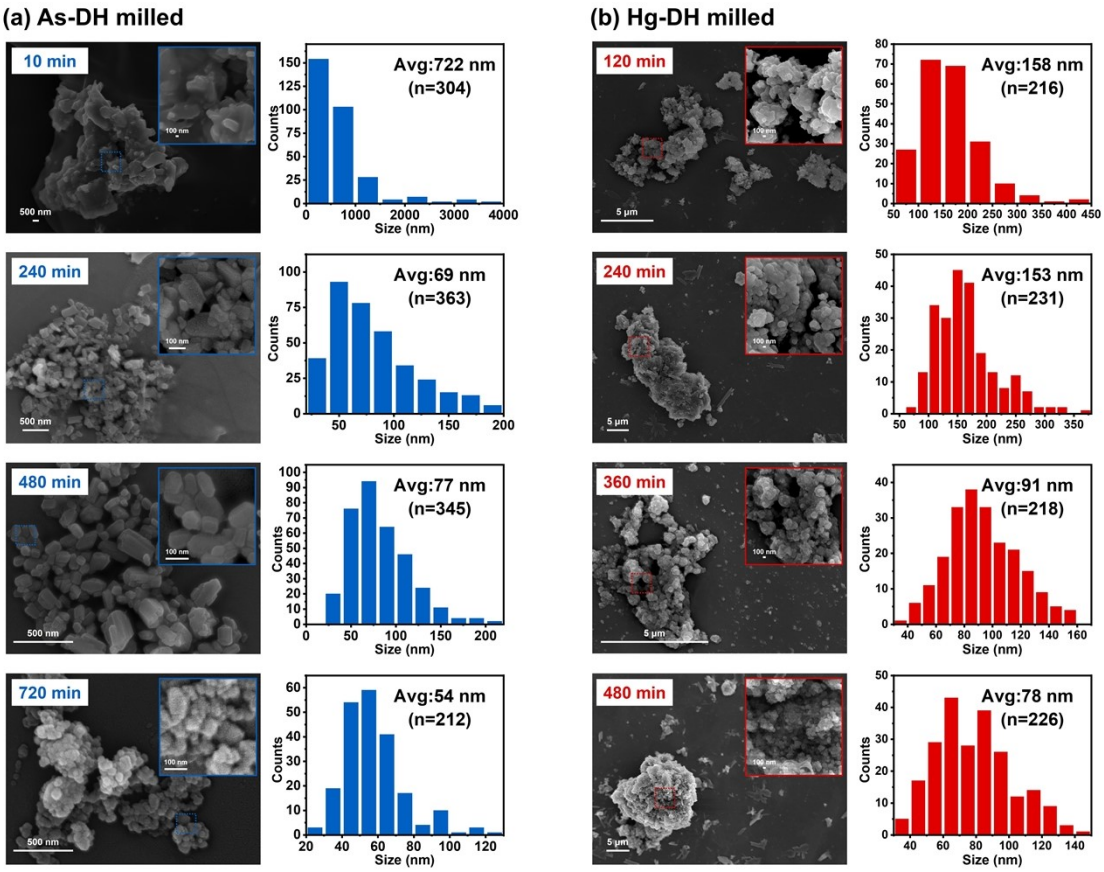

257

258 **Figure.S13** SEM images and particle size distributions of the milled products for (a)As-DH

259 and (b)Hg-DH.

260

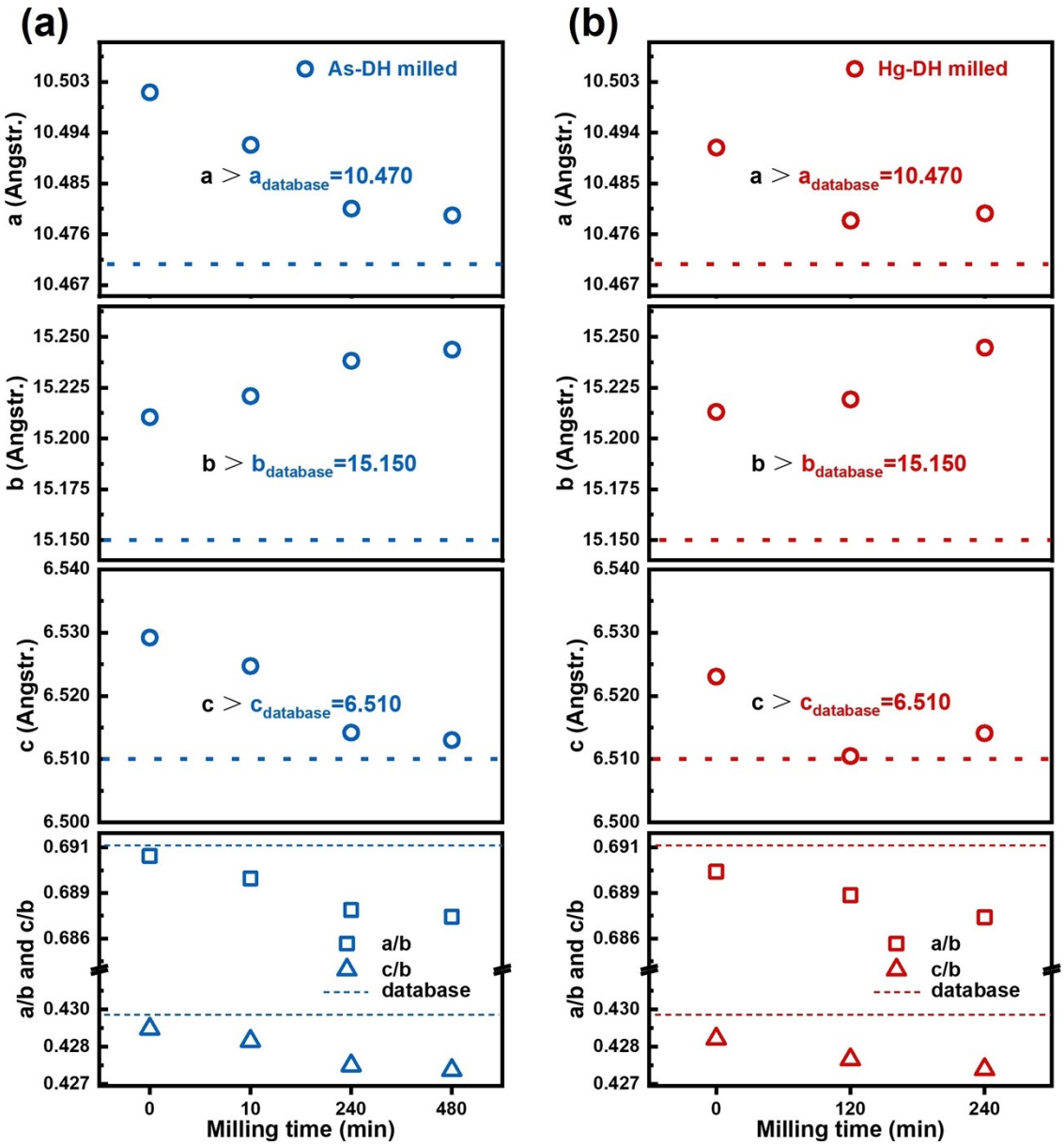

261

262 **Figure S14.** Evolution of the lattice parameters with the milling time for (a) As-DH and (b)

263 Hg-DH. The dashed lines indicate the values from the ICDD database, gypsum 01-072-0596.

264

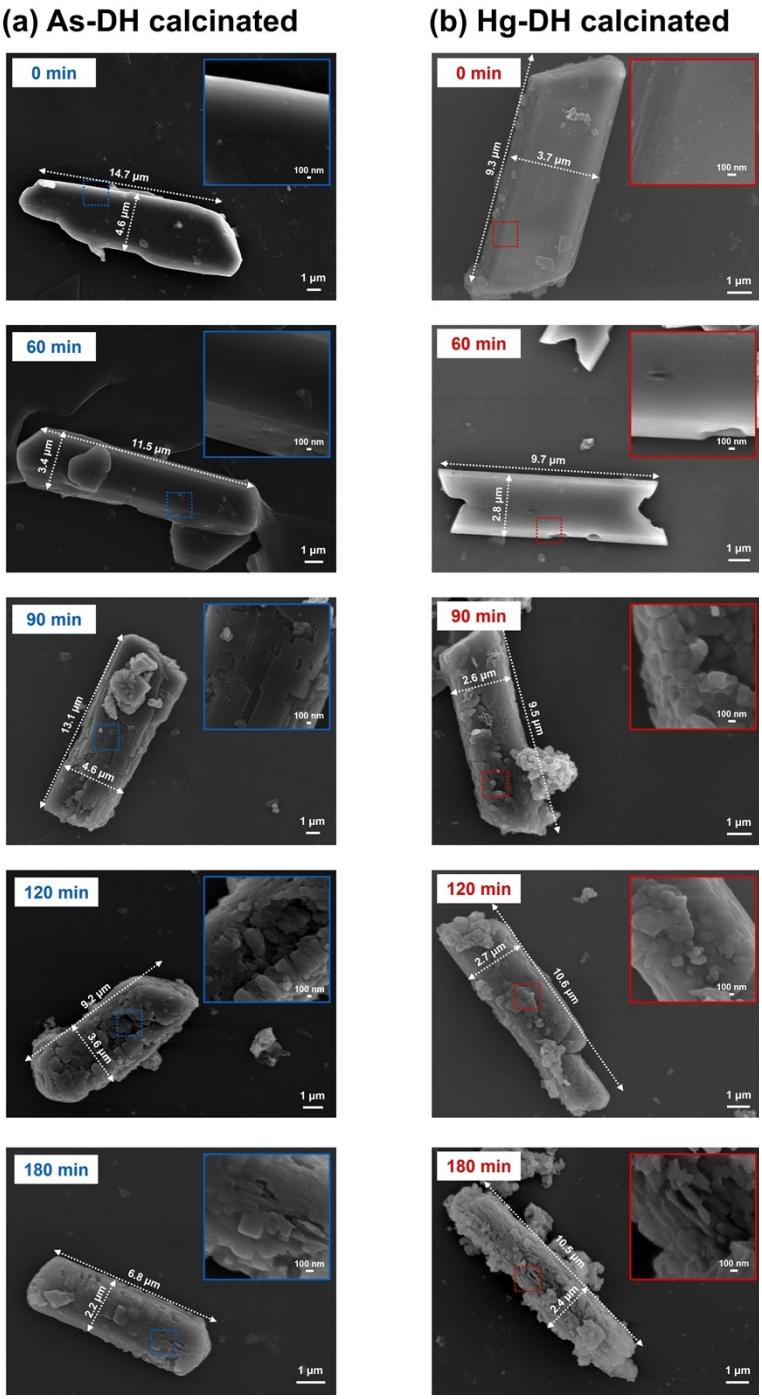

265

266 **Figure.S15** SEM images of the calcinated products for (a)As-DH and (b)Hg-DH.

267

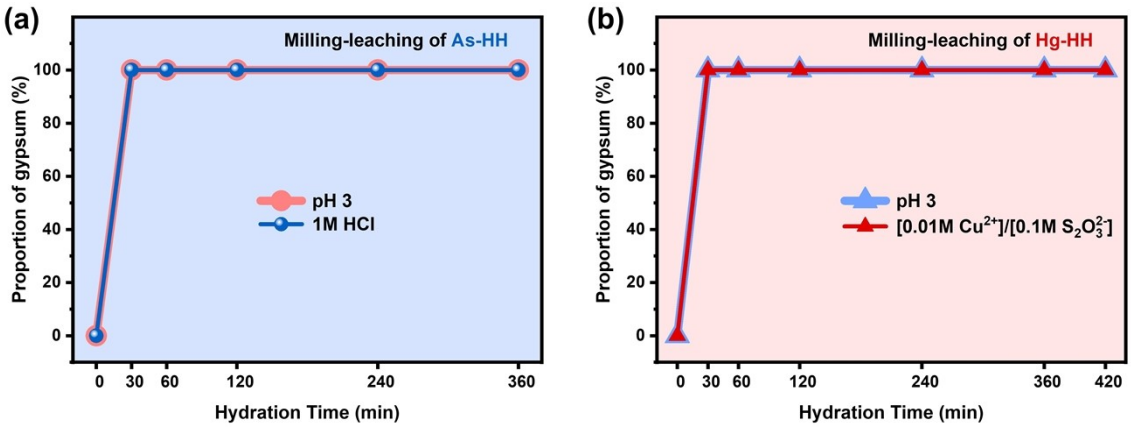

Figure S16. The proportion of gypsum in the hydration products of (a) As-HH and (b) Hg-HH obtained by ball-milling in pH=3, 1M HCl or [0.01M Cu^{2+}]/[0.1M $S_2O_3^{2-}$] solution.

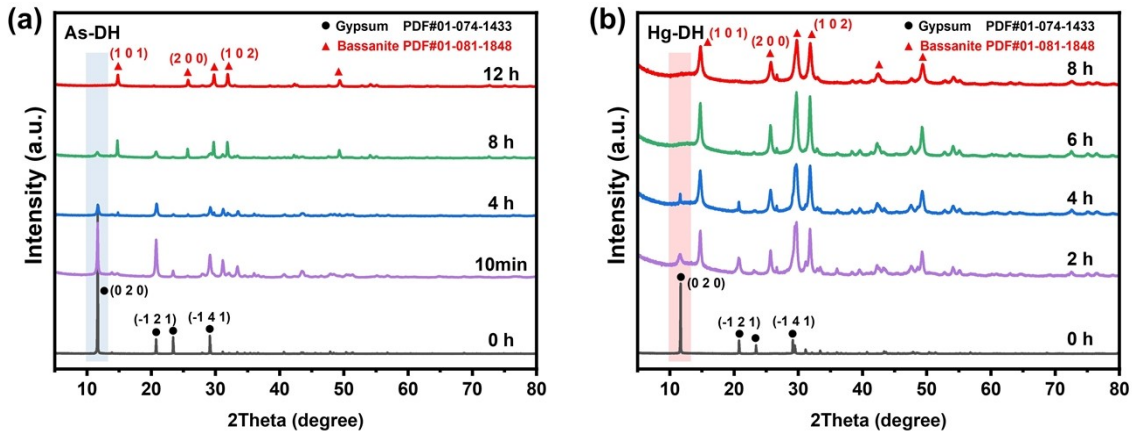

Figure S17. XRD patterns of the phases of (a) As-DH and (b) Hg-DH milled for different times.

Milled As-HH: As shown in Figure S18a, the fitted $3d_{5/2}$ peak for As^{5+} appears at approximately 44.7 eV, while the $3d_{5/2}$ peak for As^{3+} is located at around 44.2 eV. These peak positions are in agreement with the corresponding peaks in the As-gypsum (Figure S6a), indicating that arsenic primarily exists in its pentavalent form, likely as $HAsO_4^{2-}$.

Milled Hg-HH: As depicted in Figure S18b, the deconvoluted Hg 4f spectrum shows that the Hg^{2+} $4f_{7/2}$ peaks are located at 100.04 eV and 102.11 eV, while the $4f_{5/2}$ peak appears at 104.04 eV. These values align with literature values for mercury compounds, indicating that mercury remains primarily in the Hg^{2+} state as raw Hg-gypsum (Figure S6f), with no significant changes in its valence state during the milling process.

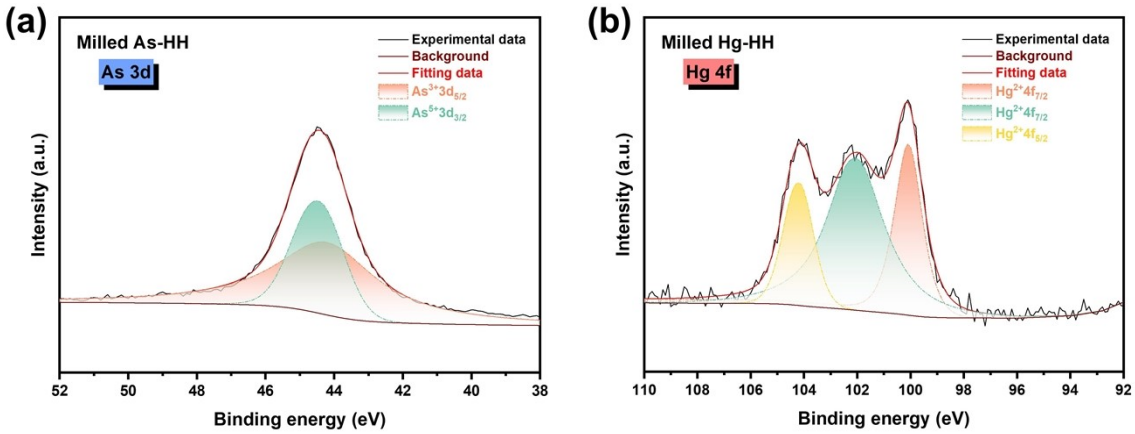

Figure S18. XPS spectra of (a) As-HH and (b) Hg-HH obtained by ball-milling.

Tables

Table S1. Origins of gypsum samples.

Gypsum samples	Place of production	Origin
P-gyp	HuBei DongSheng Chemical Group	Byproduct of phosphoric acid production
Cr-gyp	CNSIG Inner Mongolia Chemical Industry Co., Ltd., Inner Mongolia, China.	The treatment of chromium-containing wastewater in chlorate industry
As-gyp	Henan Province, China	The precipitate residue obtained during the wastewater treatment process in a copper smelting plant.
Sr-gyp	Minqin County, Gansu Province, China	The natural desert rose
Cd-gyp	Laboratory synthesis	/
Hg-gyp	Jinchuan Group Co., Ltd., Baiyin City, Gansu Province, China	In the process of acetylene production, typically achieved through the reaction of acid with calcium carbide, the precipitate residue obtained from treating acidic wastewater with calcium hydroxide.

Table S2. Incorporation amount of P, Cr, As, Sr, Cd, and Hg in calcium sulphate dihydrate.

Items	HPO_4^{2-}	CrO_4^{2-}	$HAsO_4^{2-}$	Sr^{2+}	Cd^{2+}	Hg^{2+}
M-XRD[a] (%)	4.76	1.19	2.85	0.020	0.050	0.15
M-XRD[b] (%)	0.82	0.35	1.47	0.0099	0.033	0.17
M-total[c] (%)	0.92	0.42	3.06	0.058	0.059	0.75

[a] Atomic incorporation ratio obtained by Rietveld refinement of XRD.

[b] Mass amount of metal incorporation (e.g. As or Hg) is obtained through Rietveld refinement of XRD.

[c] Metal-total values are obtained from ICP–MS analysis.

297 **Table S3.** As extraction rates of gypsum wastes with different treatments.

Treating method	Reagent	Concentration or Volume of addition	Temperature (℃)	Reaction time (h)	Extraction efficiency	References
Milling-leaching	H_2SO_4	0.50M	25	6	99.80%	Our work
Leaching in bulk solution	H_2SO_4	5.62M	30	24	50.30%	Journal of Hazardous Materials, 2024, 469, 134027
Nanoscale sulfuric acid film	H_2SO_4	5.62M	50	12	99.30%	Journal of Hazardous Materials. 2024. 469. 134027.
Conventional leaching	H_2SO_4	1.68M	65	1	79.67%	Journal of Cleaner Production. 2022. 381. 135163.
Ultrasound-enhanced sulfuric acid	H_2SO_4	1.68M	65	1	97.07%	Journal of Cleaner Production. 2022. 381. 135163.
Hydrothermal recrystallization	HCl or H_2SO_4	6.00M	120	24	99.60%	Chemosphere. 2020. 250. 126290.
Roasting	Anthracite	10 wt%	850	1	90.00%	Chemosphere. 2022. 296. 134078.

298

299

300 **Table S4.** Hg extraction rates of solid-wastes with different treatments.

Treating method	Reagent	Concentration	Temperature (°C)	Reaction time (h)	Extraction efficiency	References
Milling-leaching	$[Cu^{2+}]/[S_2O_3^{2-}]$	[0.01M]/[0.1M]	25	7	99.15%	Our work
Iodide solution system	[KI]/[NaClO]	[0.1M]/[0M]	40	1	81.22%	Journal of Hazardous Materials. 2019. 363. 179-186.
Iodide solution system	[KI]/[NaClO]	[0.1M]/[0.4M]	40	1	99.00%	Journal of Hazardous Materials. 2019. 363. 179-186.
Iodide solution system	[KI]/[NaClO]	[0.1M]/[0M]	40	1	58.24%	Journal of Hazardous Materials. 2019. 363. 179-186.
Iodide solution system	[KI]/[NaClO]	[0.1M]/[0.4M]	40	1	96.00%	Journal of Hazardous Materials. 2019. 363. 179-186.
Leaching with cuprous-thiosulfate solutions	$[Cu^{2+}]/[S_2O_3^{2-}]$	[0.01M]/[0.1M]	44	7	92.37%	Separation and Purification Technology. 2017. 177. 223-232.
Direct leaching	$[Cu^{2+}]/[S_2O_3^{2-}]$	[0.2M]/[0.1M]	45	6	85.68%	A Fundamental Study on Thiosulfate Leachingand Recovery of Mercury-bearing Solid Waste. 2019.06

301
302

303

304 **Table S5.** Standard Gibbs free energies of formation for various compounds.

Ionic (group)	**ΔG_f (kJ·mol^{-1})**
Cu^{+}	50.0
Cu^{2+}	65.5
Hg^{2+}	164.4
$S_2O_3^{2-}$	-552.5
$S_4O_6^{2-}$	-1037.5

305

306

References

1 W. Liu, J. Zheng, X. Ou, X. Liu, Y. Song and C. Tian*, et al.*, Effective Extraction of Cr(VI) from Hazardous Gypsum Sludge via Controlling the Phase Transformation and Chromium Species, *Environ. Sci. Technol.*, 2018, **52**(22), 13336-13342.

2 K. Burke, M. Ernzerhof and J. P. Perdew, Generalized Gradient Approximation Made Simple, *Phys. Rev. Lett.*, 1996, **77**(18), 3865-3868.

3 G. Kresse and D. Joubert, From ultrasoft pseudopotentials to the projector augmented-wave method, *Phys. Rev. B*, 1999, **59**(3), 1758-1775.

4 S. Grimme, J. Antony, S. Ehrlich and H. Krieg, A consistent and accurate ab initio parametrization of density functional dispersion correction (DFT-D) for the 94 elements H-Pu, *The Journal of Chemical Physics*, 2010, **132**(15), 154104.

5 E. van der Voort and P. Hartman, The habit of gypsum and solvent interaction, *J. Cryst. Growth*, 1991, **112**(2), 445-450.

6 X. Zhang, J. Wang, J. Wu, X. Jia, Y. Du and H. Li*, et al.*, Phase- and morphology-controlled crystallization of gypsum by using flue-gas-desulfurization gypsum solid waste, *J. Alloy. Compd.*, 2016, **674**, 200-206.

7 G. S. James, Lange's handbook of chemistry, *CD & W Inc, Wyoming*, 2005.

8 C. Han, W. Wang, F. Xie and T. Zhang, Mechanism and kinetics of mercuric sulfide leaching with cuprous-thiosulfate solutions, *Sep. Purif. Technol.*, 2017, **177**, 223-232.

9 K. S. Siow, L. Britcher, S. Kumar and H. J. Griesser, XPS study of sulfur and phosphorus compounds with different oxidation states, *Sains Malays.*, 2018, **47**(8), 1913-1922.

10 S. Komai, M. Hirano and N. Ohtsu, Spectral analysis of Sr 3d XPS spectrum in Sr-containing hydroxyapatite, *Surf. Interface Anal.*, 2020, **52**(12), 823-828.

11 E. Desimoni, C. Malitesta, P. G. Zambonin and J. C. Rivière, An x-ray photoelectron spectroscopic study of some chromium–oxygen systems, *Surf. Interface Anal.*, 1988, **13**(2-3), 173-179.

12 H. Zhai, L. Wang, J. Hövelmann, L. Qin, W. Zhang and C. V. Putnis, Humic Acids Limit the Precipitation of Cadmium and Arsenate at the Brushite–Fluid Interface, *Environ. Sci. Technol.*, 2019, **53**(1), 194-202.

13 Z. Ren, L. Wang, H. Wang, F. Gao, S. Liu and J. Ren, Synergistic solidification/stabilization mechanism of cadmium in phosphogypsum slag-based cementitious material, *Constr. Build. Mater.*, 2023, **400**, 132802.

14 V. I. Nefedov, Y. V. Salyn, P. M. Solozhenkin and G. Y. Pulatov, X-ray photoelectron study of surface compounds formed during flotation of minerals, *Surf. Interface Anal.*, 1980, **2**(5), 170-172.

15 P. Humbert, An XPS and UPS photoemission study of HgO, *Solid State Commun.*, 1986, **60**(1), 21-24.

16 Y. Liu, A. Wang and J. J. Freemen, 40th Annual Lunar and Planetary Science Conference, 2009.

17 J. L. Bishop, M. D. Lane, M. D. Dyar, S. J. King, A. J. Brown and G. A. Swayze, Spectral properties of Ca-sulfates: Gypsum, bassanite, and anhydrite, *Am. Miner.*, 2014, **99**(10), 2105-2115.

18 P. S. R. Prasad, Direct formation of the γ-CaSO4 phase in dehydration process of gypsum: In situ FTIR study, *Am. Miner.*, 2005, **90**(4), 672-678.

19 Z. Zheng, C. Weng, Z. Kang, M. Zhong, C. Yu and Z. Lin*, et al.*, Recycling industrial byproduct

gypsum for use as plastering materials by the tandem pyro-hydro process: impurities removal, whiteness improvement, and regularity of phase evolution, *J. Mater. Cycles Waste Manag.*, 2024.
20 P. Sayan, S. Titiz-Sargut and B. Avcı, Effect of trace metals on reactive crystallization of gypsum, *Cryst. Res. Technol.*, 2007, **42**(10), 961-970.
21 S. Wang, D. Zhang, X. Ma, G. Zhang, Y. Jia and K. Hatada, Spectroscopic and DFT study on the species and local structure of arsenate incorporated in gypsum lattice, *Chem. Geol.*, 2017, **460**, 46-53.
22 A. Pouria, H. Bandegani, M. Pourbaghi-Masouleh, S. Hesaraki and M. Alizadeh, Physicochemical Properties and Cellular Responses of Strontium-Doped Gypsum Biomaterials, *Bioinorg. Chem. Appl.*, 2012, **2012**, 1-9.
23 X. Ma, M. A. Gomez, Z. Yuan, R. Bi, J. Zhang and S. Wang*, et al.*, Incorporation of trace metals Cu, Zn, and Cd into gypsum: Implication on their mobility and fate in natural and anthropogenic environments, *Chem. Geol.*, 2020, **541**(119574), 119574.
24 Y. Yan, X. Dong, X. Sun, X. Sun, J. Li and J. Shen*, et al.*, Conversion of waste FGD gypsum into hydroxyapatite for removal of Pb2+ and Cd2+ from wastewater, *J. Colloid. Interface. Sci.*, 2014, **429**, 68-76.
25 M. Sun, J. Hou, G. Cheng, S. A. Baig, L. Tan and X. Xu, The relationship between speciation and release ability of mercury in flue gas desulfurization (FGD) gypsum, *Fuel*, 2014, **125**, 66-72.
26 A. M. Hussein, F. S. Madkour, H. M. Afifi, M. Abdel-Ghani and M. Abd Elfatah, Comprehensive study of an ancient Egyptian foot case cartonnage using Raman, ESEM-EDS, XRD and FTIR, *Vib. Spectrosc.*, 2020, **106**, 102987.
27 K. Dostert, C. P. O'Brien, W. Liu, W. Riedel, A. Savara and A. Tkatchenko*, et al.*, Adsorption of isophorone and trimethyl-cyclohexanone on Pd(111): A combination of infrared reflection absorption spectroscopy and density functional theory studies, *Surf. Sci.*, 2016, **650**, 149-160.
28 J. D. Ramsey, L. Xia, M. W. Kendig and R. L. Mccreery, Raman spectroscopic analysis of the speciation of dilute chromate solutions, *Corros. Sci.*, 2001, **43**(8), 1557-1572.
29 T. Akyuz, S. Akyuz and A. Gulec, Elemental and spectroscopic characterization of plasters from Fatih Mosque-Istanbul (Turkey) by combined micro-Raman, FTIR and EDXRF techniques, *Spectrochimica Acta Part A: Molecular and Biomolecular Spectroscopy*, 2015, **149**, 744-750.
30 S. Das, J. Essilfie-Dughan and M. J. Hendry, Fate of adsorbed arsenate during phase transformation of ferrihydrite in the presence of gypsum and alkaline conditions, *Chem. Geol.*, 2015, **411**, 69-80.
31 P. S. R. Prasad, N. Ravikumar, A. S. R. Krishnamurthy and L. P. Sarma, Role of impurities in gypsum– bassanite phase transition: A comparative Raman study, *Curr. Sci.*, 1998, **75**(12), 1410-1414.
32 C. Zou, Z. Shi, Y. Yang, J. Zhang, Y. Hou and N. Zhang, in *Minerals*, 2023, vol. 13.
33 Y. Wan, X. Wang, W. Hu, I. Chou, X. Wang and Y. Chen*, et al.*, In situ optical and Raman spectroscopic observations of the effects of pressure and fluid composition on liquid–liquid phase separation in aqueous cadmium sulfate solutions (≤400°C, 50MPa) with geological and geochemical implications, *Geochim. Cosmochim. Acta*, 2017, **211**, 133-152.
34 M. De La Pierre, C. Carteret, L. Maschio, E. André, R. Orlando and R. Dovesi, The Raman spectrum of CaCO3 polymorphs calcite and aragonite: A combined experimental and computational study, *The Journal of Chemical Physics*, 2014, **140**(16), 164509.